





Article

Identifying a Leading Predictor of Arctic Stratospheric Ozone for April Precipitation in Eastern North America

Xuan Ma ¹, Fei Xie ^{1,*} , Xiaosong Chen ¹, Lei Wang ²  and Guanyu Yang ³¹ School of Systems Science, Beijing Normal University, Beijing 100875, China² Department of Atmospheric and Oceanic Sciences, Institute of Atmospheric Sciences, Fudan University, Shanghai 200438, China³ Innovation and Research Institute of HIWING Technology Academy, Beijing 100074, China

* Correspondence: xiefei@bnu.edu.cn

Abstract: An analysis of the relationship between changes in Arctic stratospheric ozone (ASO) and precipitation in eastern North America (38°–54°N, 65°–87°W; PENA) was performed using observational and reanalysis data coupled with the Whole Atmosphere Community Climate Model version 4 (WACCM4). We found that March ASO exhibits a strong correlation with PENA in April, indicating that the one-month leading ASO exerts a potentially strong impact on April PENA. Changes in tropospheric circulation over the North Pacific and North America can be influenced by ASO anomalies via stratosphere–troposphere interactions. Increased ASO typically results in the transport of drier, colder air from northwest to eastern North America and suppresses local convective activity by enhancing regional downwelling. These conditions lead to a decrease in regional atmospheric water vapor content (1000–600 hPa). Abnormally high ASO may therefore suppress precipitation, whereas abnormally low ASO serves to enhance precipitation, and the finding is supported by WACCM4 simulations incorporating these ASO anomaly signals. We also present an ASO-based statistical linear model for predicting April PENA. Results confirm that the linear model reproduces April PENA for both training and testing periods, based on March ASO, demonstrating the reliability and stability of this linear model. This study verifies that ASO is a viable predictor for projecting April PENA and thus improving forecasts of regional seasonal precipitation.

Keywords: Arctic stratospheric ozone; precipitation; prediction; WACCM; statistical linear model



Citation: Ma, X.; Xie, F.; Chen, X.; Wang, L.; Yang, G. Identifying a Leading Predictor of Arctic Stratospheric Ozone for April Precipitation in Eastern North America. *Remote Sens.* **2022**, *14*, 5040. <https://doi.org/10.3390/rs14195040>

Academic Editor: Manuel Antón

Received: 31 August 2022

Accepted: 7 October 2022

Published: 9 October 2022

Publisher's Note: MDPI stays neutral with regard to jurisdictional claims in published maps and institutional affiliations.



Copyright: © 2022 by the authors. Licensee MDPI, Basel, Switzerland. This article is an open access article distributed under the terms and conditions of the Creative Commons Attribution (CC BY) license (<https://creativecommons.org/licenses/by/4.0/>).

1. Introduction

Changes in precipitation can interfere with a wide range of natural processes and have considerable social and economic significance. Eastern North America—including the northeastern United States and southeastern Canada—frequently experiences meteorological and climatic disasters and, in recent decades, has become significantly wetter than the long-term average [1]. For example, the National Centers for Environmental Information reported that April 2010 was the 13th driest April in the northeastern United States since recordkeeping began in 1895. April 2011 was the second wettest April in the northeastern United States in 117 years. These events caused huge economic losses and casualties [2,3]. Numerous studies demonstrate that precipitation in eastern North America (PENA) has changed significantly over the last few decades [4–12]. In the northeastern United States, for instance, both the intensity of precipitation and frequency of precipitation events have increased measurably [13–18], and Zhang et al. [5] reported more frequent springtime heavy rainfall events over eastern Canada.

Previous studies have demonstrated how PENA can be modulated by multiple factors [19–31], including the El Niño–Southern Oscillation [32], severe storm events [33], the Pacific–North American pattern [34,35], the North Atlantic Oscillation [34,36] and Atlantic Multidecadal Oscillation [37], and the Pacific Decadal Oscillation [38]. Nevertheless, these

factors are all from the troposphere, and the climate of North America at mid- to high-latitudes (north of 60°N), is easily affected by the Arctic stratospheric circulation. However, the Arctic stratospheric factors related to PENA has not received sufficient attention.

Model simulations and observational data both suggest that circulation anomalies related to anomalies in springtime Arctic stratosphere ozone (ASO) can propagate downward, ultimately reaching the surface and influencing surface temperature [39,40]. For instance, Hu and Tung [41] and Hu et al. [42] found that warming of surface air temperatures over Eurasia since the late 1970s is strongly correlated with Arctic ozone depletion, and Smith and Polvani [43] and Calvo et al. [39] demonstrated that North Atlantic precipitation can also be modulated by Arctic ozone variability. Based on simulations by the European Centre/Hamburg version 5 (ECHAM5) atmospheric general circulation model, Karpechko et al. [44] revealed an obvious tropospheric climate response to the 2011 ozone depletion and sea surface temperature anomalies. The Arctic stratospheric polar vortex plays a key role in the ASO and tropospheric precipitation. Previous studies have shown that Arctic stratospheric polar vortex changes could affect the precipitation in the tropics and subtropics [45,46], and in the northern middle latitudes [47,48]. Anomalously strong or weak polar vortex states correspond to positive or negative phases of the stratospheric Northern Annular Mode, respectively, and these can lead to positive or negative tropospheric Arctic Oscillation (AO) events, which can subsequently alter patterns of surface precipitation [49–54]. For example, Zhang et al. [48] found more precipitation in the northwestern North Pacific in late winter and spring during weak polar vortex events than during strong polar vortex events. Subsequently, using various datasets, Zhang et al. [55] pointed out that during weak polar vortex events, precipitation rates over the western and southeastern parts of North Pacific, the southern part of North Atlantic, and Southern Europe are larger, whereas the total precipitation rates over the central North Pacific, the northern parts of North Atlantic, and Northern Europe are smaller than those during strong stratospheric polar vortex events. As our understanding of stratosphere–troposphere coupling improves, various researchers have focused on the role of ozone in seasonal forecasting [44,56,57]. Based on observations and chemistry–climate models, Stone et al. [57] constructed a linear regression model to predict April surface temperature based on March ASO; their results suggested that April surface temperature can be predicted for four years in individual ensemble members and for six years using observations extending beyond the regression model. Similarly, Xie et al. [58] employed February–March ASO and Indian Ocean sea surface temperature data to establish a linear regression model for predicting April–May precipitation in central China, with a lead time of 1–2 months.

As mentioned above, the majority of current PENA predictions incorporate the tropospheric signals described above; stratospheric signals, in contrast, are largely ignored. However, the potential link between PENA and stratospheric anomalies remains an open question. We seek to address this issue by exploring the possible mechanisms controlling the impact of ASO on PENA, and the potential for making ASO-based predictions of PENA on a seasonal basis. The remainder of this paper is organized as follows: Data, methods, and experiment design are described in Section 2; Section 3 presents the physical mechanisms underlying the ASO–PENA relationship, based on observational and reanalysis data; Section 4 provides the precipitation response to ASO anomalies, based on WACCM4 and linear regression modeling; Section 5 presents our conclusions.

2. Data, Simulations, and Methods

2.1. Data

Monthly mean ozone data were sourced from the Stratospheric Water and Ozone Satellite Homogenized (SWOOSH) database, which includes vertically resolved ozone and water vapor data from a subset of the limb profiling satellite instruments operating since the 1980s [59]. Ozone data used in this study have a horizontal resolution of $2.5^\circ \times 2.5^\circ$ with 31 vertical levels (316–1 hPa). To demonstrate the results are not simply artifacts of a particular dataset, we also employed the Global Ozone Chemistry and Related trace gas

Data Records for the Stratosphere (GOZCARDS) project [60] ozone data, which have a horizontal resolution of $10^\circ \times 10^\circ$ with 25 levels (surface to 0.1 hPa). Ozone data from SWOOSH agree with those from GOZCARDS [61]. Further, an ASO index was defined to analyze the relationship between ozone and tropospheric precipitation. It is the zonal mean ozone column abundance in Dobson Unit (DU) averaged over the area for the latitude of $60\text{--}90^\circ\text{N}$ at an altitude of 100–50 hPa (~1.6–21 km) after removing the seasonal cycle and long-term linear trend for 1985–2019.

Precipitation was obtained from the Global Precipitation Climatology Project (GPCP), which is a merged product (with 2.5° horizontal resolution) of rain gauge measurements, satellite retrievals, and numerical model outputs [62]. To demonstrate the robustness of the results, we also employed precipitation from the Global Precipitation Climatology Centre, which is calculated from global station data (with 1.0° horizontal resolution) in this study [63]. Total cloud cover data were taken from the European Centre for Medium-range Weather Forecasts reanalysis 5, ERA5 [64]. Monthly mean winds, geopotential height, and other meteorological fields were taken from the National Centers for Environmental Prediction–National Center for Atmospheric Research (NCEP–NCAR) Reanalysis-II (NCEP2) [65]. All these datasets for the period of 1985–2019 were analyzed except for the GOZCARDS data, which are only updated to 2012.

2.2. Simulations

The Whole Atmosphere Community Climate Model, version 4 (WACCM4) [66], as an atmospheric component of the coupled-climate-system model—Community Earth System Model (CESM) version 1.0.6, was used in this study. It uses a finite-volume dynamical core and has 66 vertical levels extending from the surface to 5.1×10^{-6} hPa (~140 km). The simulations presented in this paper were run at a horizontal resolution of $1.9^\circ \times 2.5^\circ$ (latitude \times longitude) and the inactive chemistry was disabled in the simulations [67]. The vertical resolution is 1.1–1.4 km in the tropical tropopause layer and lower stratosphere.

Three experiments were designed to investigate the response of PENA to ASO anomalies. All the model simulations were run using greenhouse gas (GHG) values from emissions scenario A2 of the Intergovernmental Panel on Climate Change [68] for 1995–2005. The Quasi-Biennial Oscillation (QBO) forcing was prescribed with a 28-month fixed cycle. Only the ozone forcing from CMIP5 ensemble mean ozone output over the period 1995–2005 was different among the three simulations. The control run, E1, used a 12-month seasonal cycle of ozone forcing, averaged over the period 1995–2005. E2 was the same as E1, except that the March ozone in the region of $45\text{--}90^\circ\text{N}$ at levels between 300 and 30 hPa was decreased by 15% compared with E1. E3 was the same as E2, except that the March ozone was increased by 15% compared with E1. The above-mentioned experiments were all integrated for 43 years, with the first 3 years discarded as the model spin-up.

2.3. Leave-One-Out Validation

Leave-one-out cross-validation is a special case of cross-validation and can be used to assess the reliability of the regression model and judge whether the regression model is overfitting the data [69]. It uses one observation from the original sample as the validation data, and the remaining observations as the training data. For example, for a dataset having n rows, the 1st row is selected for validation, and the remaining $(n - 1)$ rows are used to train the model. Then, the 2nd row is selected for validation and the remainder to train the model. Similarly, the processes are repeated for n steps. This estimation method is almost unbiased and is widely used when the available data are quite rare. This process is closely related to the statistical approach of jack-knife estimation [70].

Climate prediction systems now increasingly rely on the global climate models (GCMs), but it is difficult to make reliable predictions for regional weather and climate due to their low spatial resolution. Previously, Guo et al. [71] pointed out that linear models in statistics perform well on regional seasonal forecasts and provide a clearer mechanistic explanation [72]. Thus, we establish a linear least squares regression model with ASO as a

sole predictor for April PENA in Section 4. To investigate the model's stability, data were divided into two parts: 1985–2007 for the training period and 2008–2019 for the test period. Using this regression model, modeled April PENA was fitted to the training period, and the forecast was produced for the test period to demonstrate its hindcast ability.

3. Results

3.1. Correlations between Observed ASO and PENA

Figure 1 illustrates the spatial distribution of the correlation coefficient between March ASO and April PENA. We note that a high correlation coefficient occurs throughout much of the northeastern United States and southeastern Canada, which together represent the most economically developed, densely populated, and culturally diverse region in North America. Such characteristics are prevalent in multiple datasets, indicating that these results are robust and not simply artifacts of a particular dataset. To further estimate the relationship between ASO and PENA, we calculated the monthly correlation coefficients of March ASO and monthly precipitation over the entire study area (38–54°N, 65–87°W; Figure 2a). According to this treatment, the correlation coefficient between March ASO and April PENA (−0.61) is the only value that is significant at the 95% confidence level. As shown in Figure 2b, ASO and PENA both exhibit clear interannual variability. Strong March ozone depletion events (e.g., 1993, 1996, 2000, 2011) correspond to more PENA. In contrast, strong positive ASO anomaly events correspond to less PENA accompanied by almost simultaneous SSW events (e.g., 1999, 2010). The above result suggests that the PENA response lags ASO anomalies by one month and persists for approximately one month. Since the relationship between ASO and PENA is not sensitive to the ozone and precipitation data selected in this study, hereafter we report only those findings obtained from the SWOOSH and GPCP datasets.

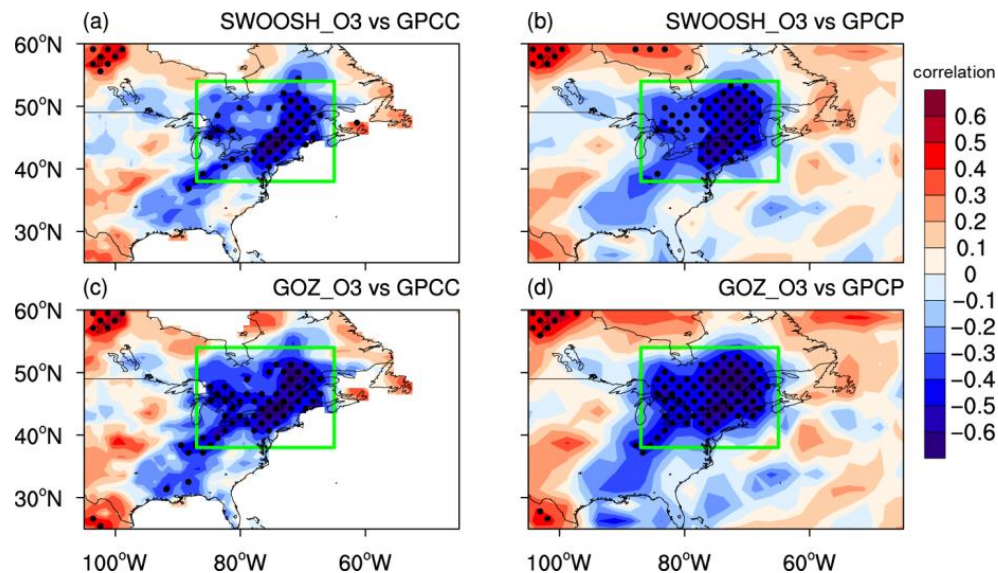


Figure 1. Correlation coefficient maps between the March ASO index and April precipitation anomalies for (a,b) 1985–2019 and (c,d) 1985–2012. ASO indices are calculated based on the (a,b) SWOOSH and (c,d) GOZCARDS datasets; precipitation data are derived from (a,c) GPCC and (b,d) GPCP. In (a–d), the long-term linear trends of the ASO index and precipitation were removed prior to the correlation analysis. Stippling denotes areas where correlation coefficients are significant at the 95% confidence level. The green square indicates the study area.

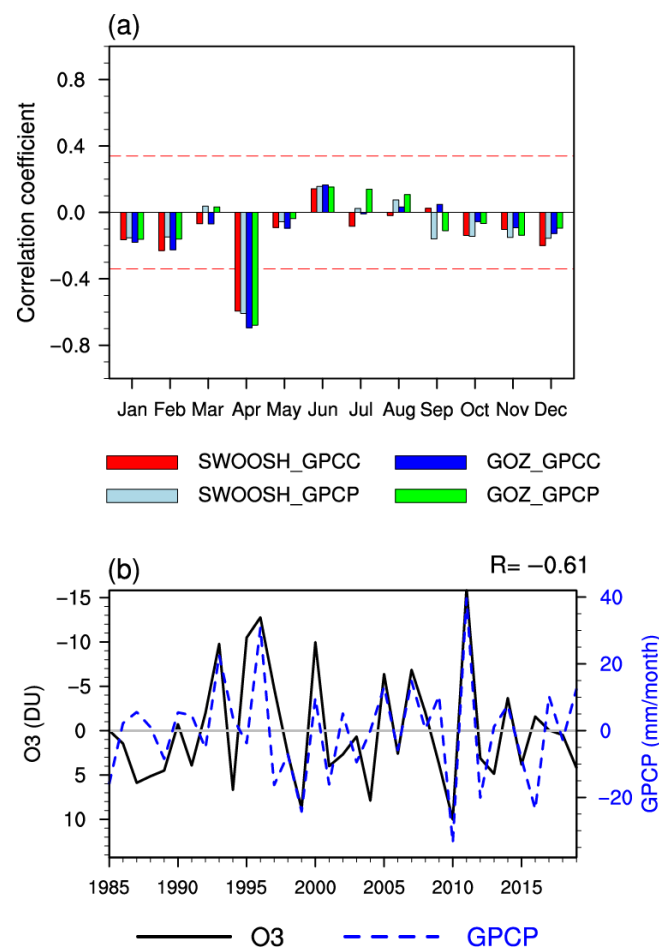


Figure 2. (a) Correlation coefficients between March ASO index and precipitation anomalies over eastern North America ($38\text{--}54^\circ\text{N}$, $65\text{--}87^\circ\text{W}$) for individual months (January–December of the same year), calculated using different ozone and precipitation datasets for the period 1985–2019 (SWOOSH). We note that the GOZCARDS ozone data span the period 1985–2012. Red lines denote correlation coefficients that are significant at the 95% confidence level. (b) Time series of March ASO index and regionally averaged April rainfall anomalies after removal of seasonal cycles and linear trends. The correlation coefficient between the two time series is given in the upper-right corner. ASO data are derived from SWOOSH and rainfall from GPCP.

Our results indicate that the one-month leading ASO anomaly has a potential impact on PENA during the subsequent April. Figure 3a depicts the difference in April precipitation anomalies over eastern North America corresponding to the occurrence of positive and negative March ASO anomaly events (Table 1). ASO-related precipitation differences averaged over the studied area can reach about -30.9 mm/month, about -38.5% of the total monthly mean (Figure 3b), suggesting that ASO plays an important role in regulating precipitation variability over eastern North America. Therefore, accurate observation of March ASO variability can be used to predict April rainfall, with important implications for reducing economic losses caused by extreme precipitation events.

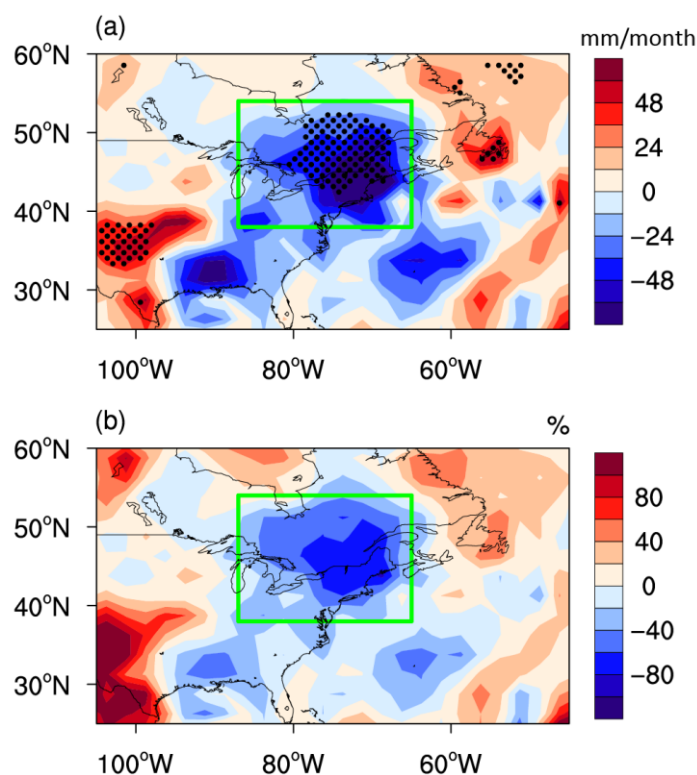


Figure 3. (a) Composite differences in April rainfall anomalies (mm/month; from GPCP) between positive and negative ASO anomaly events during 1985–2019. Detailed anomalous events can be found in Table 1. (b) Ratio of the composite differences to April precipitation climatology.

Table 1. Positive and negative ASO anomaly events during the period 1985–2019. A positive (negative) ASO anomaly event is identified when the March ASO index, calculated from SWOOSH, is greater (smaller) than 1 (−1) standard deviation.

	Positive Anomaly Events	Negative Anomaly Events
March ASO	1994, 1999, 2004, 2010	1993, 1995, 1996, 2000, 2005, 2007, 2011

3.2. The Potential Mechanisms Linking ASO and PENA

Previous studies have highlighted the delayed climatic influence of Arctic ozone on the mid- and high-latitude Northern Hemisphere [39,40,44,47,56,57,61,73,74], a pattern that can be explained via the interaction between the ASO and tropospheric circulation. It has been shown that the decrease in Arctic total column ozone (TCO) induces a decrease in shortwave heating [47,61,73–76], and thereby favors cooling and strengthening of the Arctic SPV (stratospheric polar vortex). Anomalies in March ASO could result in a circulation anomaly (North Pacific Oscillation, NPO) over the North Pacific, and the process and mechanism of ASO affecting the NPO has been analyzed in detail in previous studies. Wang et al. [77] pointed out that the intensified stratospheric circulation induces the tropospheric positive AO (+AO)-like anomaly via stratosphere–troposphere dynamical coupling, and the +AO-like anomaly is largest in late March when March ASO is abnormally low. Subsequently, the easterly anomalies over the midlatitude eastern Asia related to the +AO-like anomaly further extend eastward and favor the negative North Pacific Oscillation (−NPO)-like circulation anomaly via anomalous zonal wind shear and the interactions between synoptic scale eddies and the mean flow in early–middle April. Previously, Xie et al. [61] also depicted composite daily variations in zonal wind anomalies during positive and negative ASO events, Arctic stratospheric circulation anomalies related to ASO can propagate downward into the polar troposphere within days. Subsequently, the abnormal circulation can be observed extending into the mid-latitude North Pacific basin

over the next 30 days, suggesting that Northern Hemisphere mid-latitude tropospheric circulation could be modulated by ASO, with a lag of one month.

To further explore the physical processes of March ASO driving annual variability in April PENA, we produced horizontal spatial distributions of correlation coefficients for March ASO and the April zonal wind and geopotential height fields (Figure 4). This treatment reveals a tripolar pattern across the North Pacific (Figure 4a,c,e), consistent with the results of Wang et al. [77]. Specifically, Figure 4 demonstrates that ASO-related changes in Arctic stratospheric circulation during March can influence the circulation over the central North Pacific and even North America. Details of the mechanisms responsible for the effects of the ASO on the North Pacific can be seen in Xie et al. [61]. Consequently, high positive correlations between ASO and geopotential height variations occur over central North America (Figure 4b,d,f), implying that enhanced ASO corresponds to anomalous anticyclonic airflow over North America. This circulation will serve to enhance the transport of dry, cold air from the continental interior toward eastern North America, resulting in a significant decrease in atmospheric water vapor content over the latter.

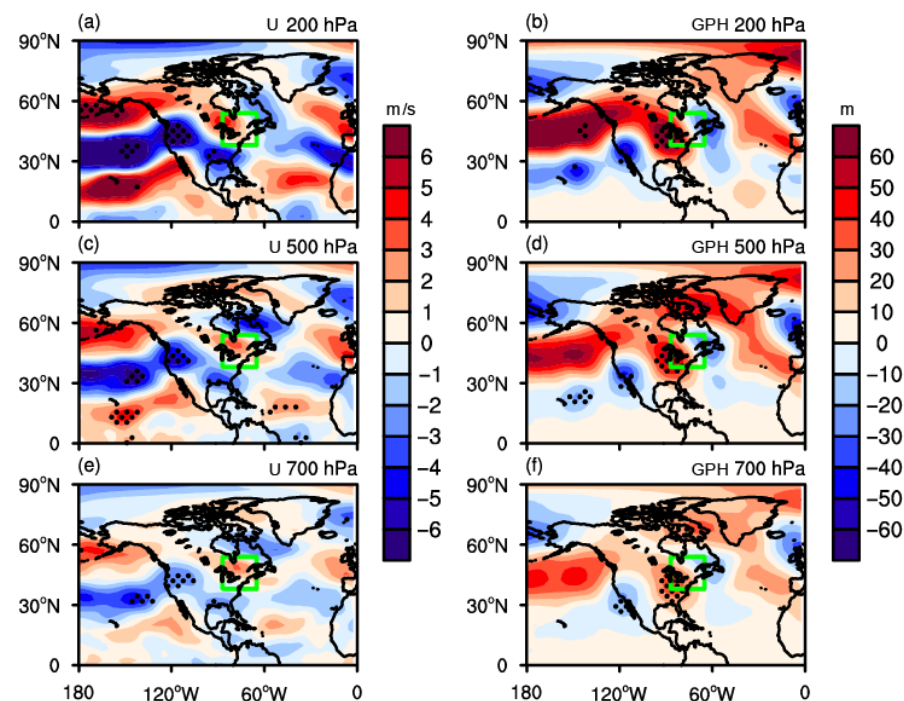


Figure 4. (a,c,e) Composite differences in April zonal wind (m/s; from NCEP2) between positive and negative ASO anomaly events during 1985–2019. (b,d,f) Same as (a,c,e), but for geopotential height. Black dots denote those regions with significant correlation coefficients at the 95% confidence level. Detailed anomalous events can be found in Table 1.

To investigate this relationship in more detail, we present the composite differences in April wind fields between positive and negative ASO anomalies. When ASO increases, we observe that climate in eastern North America is dominated by anomalous northwesterly winds (Figure 5). Since atmospheric water vapor in this region is derived primarily from the northwest, where the air is drier and colder (Figure 6a), this particular circulation pattern is not conducive to elevated water vapor concentrations over eastern North America. Figure 6c shows the water vapor flux divergence, in which the negative response of water vapor to enhanced ASO is clearly visible. As reported recently by Kunkel et al. [78], precipitation amounts over the continental United States tend to scale linearly with the water vapor content of the air column, in which case our results indicate that increased (decreased) ASO will serve to reduce (enhance) precipitation over eastern North America.

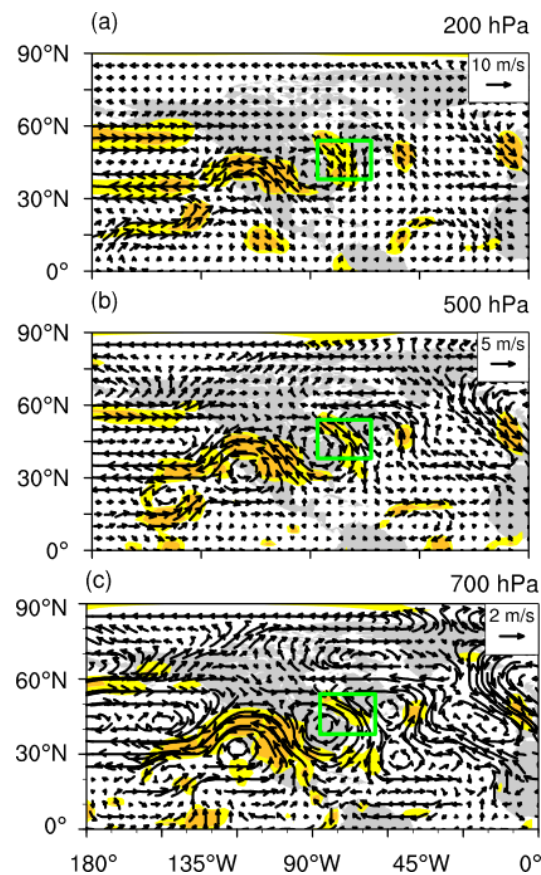


Figure 5. Composite differences in April wind (vectors, m/s; from NCEP-2) between positive and negative ASO anomaly events at (a) 200 hPa, (b) 500 hPa, and (c) 700 hPa. Light and dark yellow areas represent values that are statistically significant at the 90% and 95% confidence levels, respectively. Detailed anomalous events can be found in Table 1.

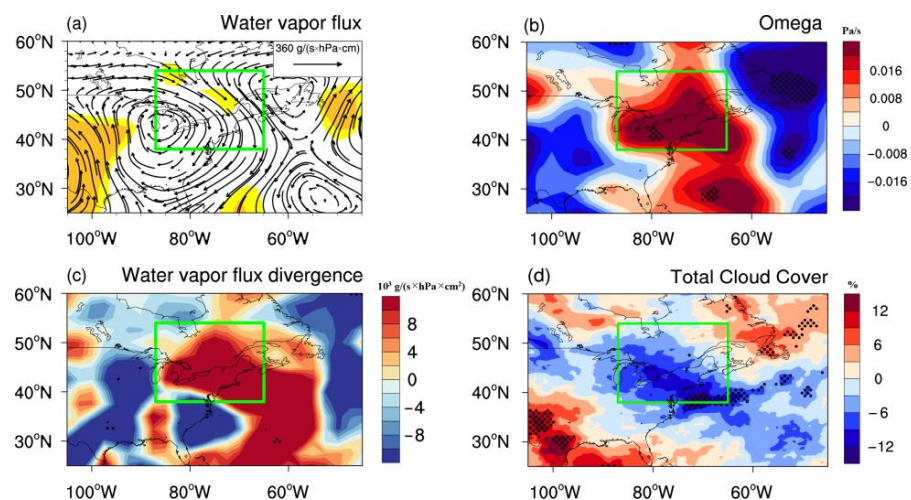


Figure 6. (a) Composite differences in April vertically integrated water vapor flux (vectors, $\text{g}/(\text{s} \times \text{hPa} \times \text{cm})$) over 1000–600 hPa between positive and negative ASO anomaly events. Light and dark yellow areas represent values that are statistically significant at the 90% and 95% confidence levels, respectively. (b–d) Same as (a), but for vertical velocity at 700 hPa (Pa/s, Red (blue) colors represent descending (ascending) motion), water vapor flux divergence (units: $10^3 \text{ g}/(\text{s} \times \text{hPa} \times \text{cm}^2)$), and total cloud cover (%), respectively. Detailed anomalous events can be found in Table 1. Black dots denote regions with correlation significant at the 95% confidence level.

The lifting and adiabatic cooling of air is a prerequisite for precipitation; when an ascending air parcel rises above the lifting condensation level, vapor condenses to form clouds, thereby creating favorable conditions for precipitation. The spatial distribution of vertical velocity anomalies associated with enhanced ASO is depicted in Figure 6b, and reveals enhanced tropospheric downwelling over eastern North America. Such changes in circulation are likely to suppress local convective activity (Figure 6b) and reduce overall precipitation. Spatial patterns of April total cloud cover also reveal a negative correlation with March ASO in this region (Figure 6d).

Existing observational data suggest that ASO affects PENA with a lead time of one month. Over the North Pacific and North America, for instance, elevated ASO impacts tropospheric circulation via the stratosphere–troposphere interaction described above. Over eastern North America, positive ASO anomalies are associated with northwesterly airflow, thereby resulting in decreased atmospheric water vapor content, weakened local convection (Figure 6b), and reduced cloud cover (Figure 6d). Such conditions ultimately lead to reduced precipitation over eastern North America. The opposite occurs under anomalously low ASO conditions.

3.3. The WACCM Results

To corroborate our proposed mechanism for ASO–PENA interactions, we simulated the response of circulation, precipitation, and radiation over eastern North America to ASO anomalies. Details of these simulations can be found in Section 2. First, we confirm that the model can reproduce North American precipitation faithfully. As shown in Figure 7, WACCM4 effectively reproduces the observed spatial distribution of climatological April rainfall; the three major precipitation centers located over the west coast, southern North America, and part of the northwestern North Atlantic are simulated realistically, underscoring the suitability of this model for our analysis. The simulated response of April PENA to ASO variability (Figure 8) reveals that modeled precipitation anomalies also show decreased precipitation over most parts of the studied area, similar to the observations. Although there are some small differences between simulated precipitation and observations, this may be because the model convection parameterization scheme over and around the Rocky Mountains is not perfect.

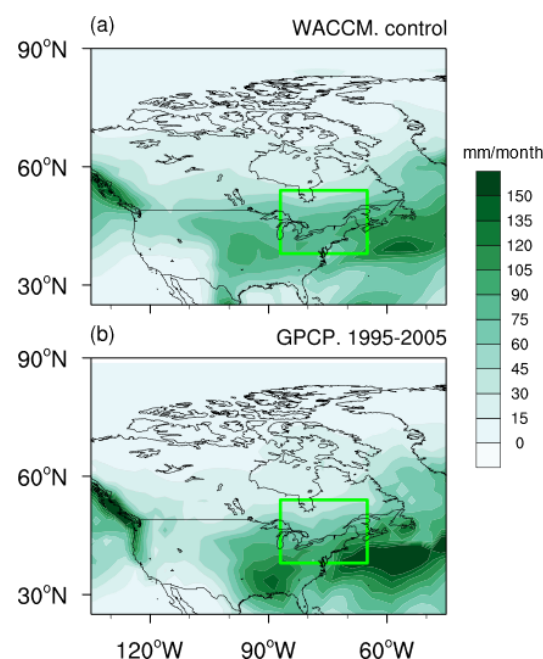


Figure 7. (a) Climatological distribution of April rainfall (mm/month) in the control experiment (E1). (b) Same as (a), but for GPCP-derived rainfall during the period 1995–2005.

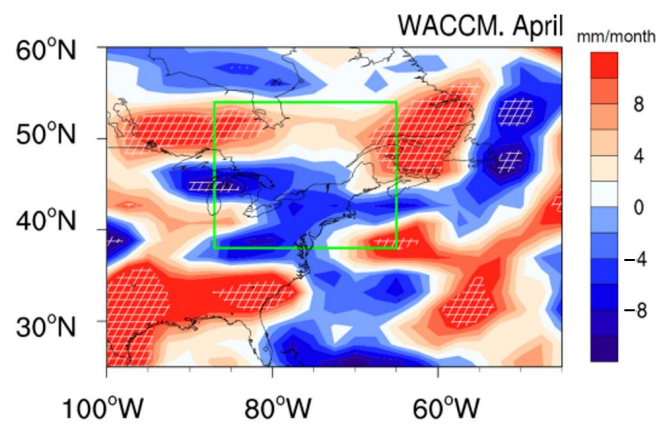


Figure 8. Differences in April precipitation between experiments E3 and E2 (mm/month). Cross-hatching denotes regions for which values are significant at the 90% confidence level.

The simulated responses of water vapor flux and its divergence to ASO anomalies are displayed in Figure 9. Over eastern North America, the water vapor flux exhibits an anticyclonic behavior (Figure 9a) that is similar to the observed conditions (Figure 6a). Although the enhanced moisture divergence is also well simulated (Figure 9c), we note that the center of divergence is displaced slightly south of its observed position (Figure 6c). This offset potentially reflects limitations in the convective parameterization scheme employed in the model, as suggested by several previous studies [79–81], particularly in the vicinity of the Rocky Mountains. The model's coarse resolution may further exacerbate simulation inaccuracies.

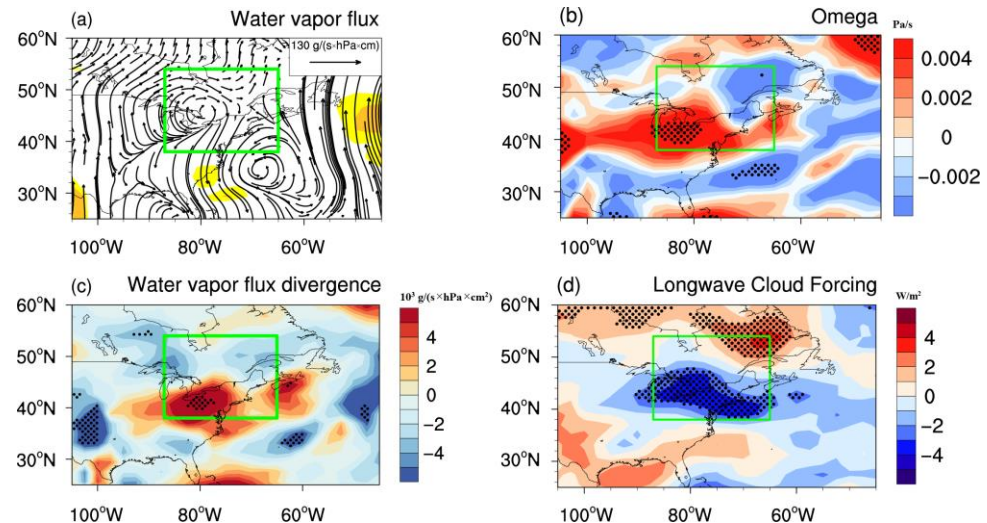


Figure 9. (a–c) Same as Figure 6a–c, but for the differences between experiments E3 and E2. Meridional water vapor flux components in (a) are multiplied by 5. (d) Long wave cloud forcing (W/m^2) between experiments E3 and E2. Black dots denote regions where differences are significant at the 90% confidence level. The experiments are based on WACCM4.

Figure 9b displays the differences in forced vertical velocity anomalies for April between E3 and E2. Changes in vertical velocity align with those depicted in Figure 6b. Negative cloud forcing is forced by an increase in ASO, suggesting that clear sky conditions and reduced cloud cover will become more common under abnormally high ASO levels. This pattern is consistent with the spatial distribution of correlation coefficients between March ASO and April cloud cover (Figure 6d), and both observed and simulated results indicate that changes in April PENA are closely related to ASO variability.

4. A Linear Regression Model for Predicting April PENA

Building upon the established relationship between March ASO and April PENA, we constructed a linear regression model that utilizes the former to predict the latter. Specifically, we established an ASO-based linear regression model for April PENA, spanning the training period 1985–2007, using the formula:

$$\text{PENA}(t) = -1.23 \times \text{ASO}(t) + 178.21 \quad (1)$$

where t is time in years. Units for April PENA and March ASO are mm and DU, respectively.

As shown in Figure 10a, variations in April PENA, fitted with the ASO-based linear regression model, reflect certain characteristics of the observed PENA. For instance, the correlation coefficient between the two is 0.59, which passes the 99% confidence level in a Student's t -test over the course of the training period. During the test period (2008–2019), the correlation coefficient is 0.69 (99% confidence level). We note that the predicted April PENA is closer to observed values during the test period, potentially reflecting the stronger relationship between ASO and PENA for that period. Further analysis will be necessary to explore this disparity further. To investigate the stability of the linear regression model and its suitability for prediction, we employed various training and test periods following the approach documented by Kim et al. [82] (Figure 10b,c). Our results indicate that fitted and predicted April PENA values are both closely correlated with observed values under different data segments. All correlation coefficients exceed 0.50 and are statistically significant at the 95% confidence level, suggesting that the empirical linear model performs well in predicting seasonal PENA.

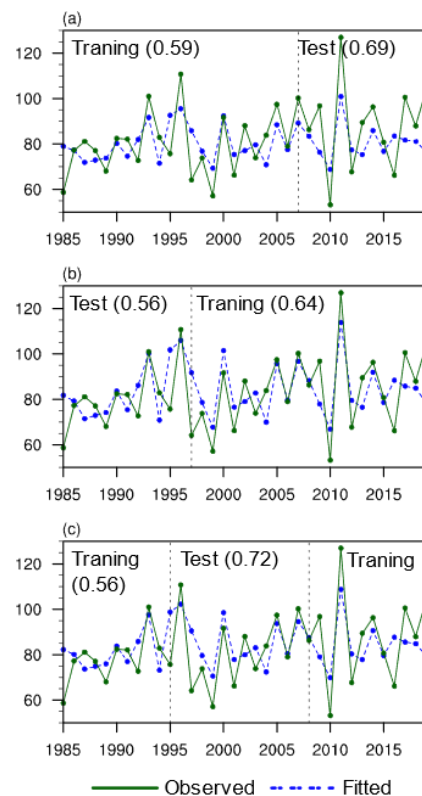


Figure 10. (a) Observed April PENA (green line, mm/month) and fitted April PENA variations (blue line, mm/month) established by the linear regression model for March ASO during 1985–2019. The training period is 1985–2007 and the independent test period is 2008–2019. (b) Same as (a), but with a training period of 1997–2019 and independent test period of 1985–1996. (c) Same as (a), but with an independent test period of 1996–2007 and the other years are used for the training period. The numbers in parentheses represent the correlation coefficients.

Acknowledging the limited temporal scale of the dataset, and to avoid overstating the efficacy of our linear regression model, we took a leave-one-out cross validation approach to evaluate model performance. Using this approach, precipitation within each grid cell is predicted based on the leave-one-out method. Specifically, leave-one-out cross validation used in this study is that the predicted precipitation for each year is predicted by a linear prediction model constructed based on data from other years, and the predicted precipitation for all years is obtained based on this method. Then, the predicted April precipitation is compared with observations. Figure 11a shows the spatial distribution of correlation coefficients between predicted and observed PENA; these data confirm that the ASO-based model can reproduce PENA effectively, producing significant positive correlations between simulated and observed values over eastern North America. The correlation coefficient between the two time series is 0.53, which passes the 99% confidence level (Figure 11b), thus indicating that our linear model is robust and suitable for predicting future precipitation.

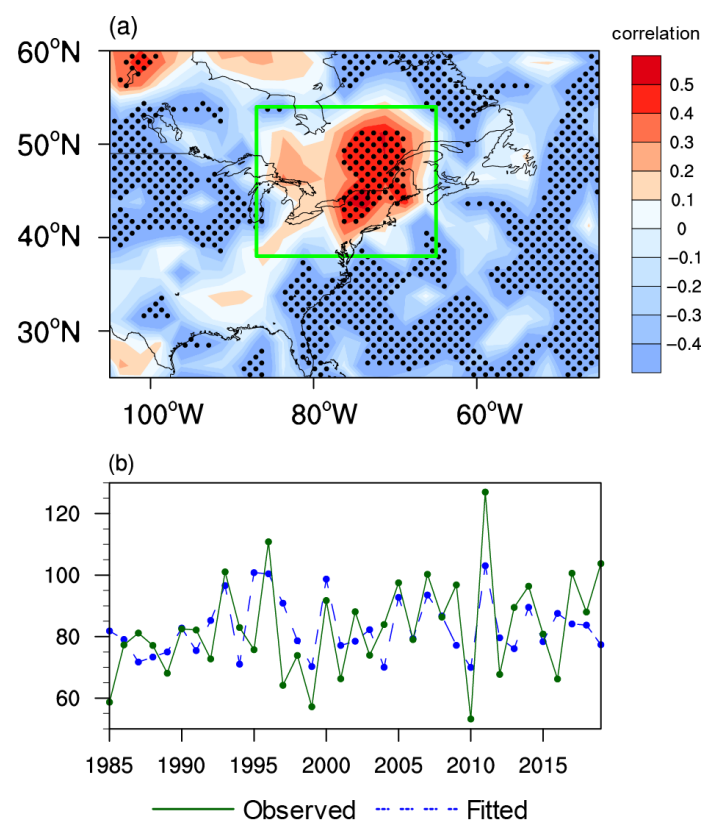


Figure 11. (a) Mapped correlations between observed and predicted April PENA variability for the period 1985–2019. Predicted April PENA was established using the linear regression model incorporating March ASO, based on the leave-one-year-out method. (b) Time series of observed April PENA (green line, mm/month) and predicted April PENA variations (blue line, mm/month) based on the leave-one-year-out method.

5. Conclusions

April PENA exhibits significant interannual variability and is strongly correlated with April ASO, but lags by one month. We find that it takes approximately one month for the ASO signal to propagate to the northern mid-latitude troposphere, a process that in turn affects regional weather and climate. These lagged, ASO-driven circulation anomalies exhibit a clear tripolar pattern over the North Pacific and result in anticyclonic circulation over central North America. During positive ASO anomaly events, these circulation anomalies cause cold, dry air to be drawn into eastern North America, resulting in relatively cool, dry conditions overall. Further, ASO-related changes in vertical velocity serve to suppress local

convective activity, thereby inhibiting cloud formation and reducing local precipitation. The opposite pattern occurs during abnormally low March ASO. This relationship is corroborated by our model tests using the WACCM4. Together, our findings indicate that the delayed impact of ASO on PENA is primarily a function of the regulation of tropospheric circulation over eastern North America.

Recognizing the delayed impact of ASO on PENA, we demonstrate that ASO can be used in the prediction of seasonal precipitation in North America. Our empirical linear model, which incorporates the one-month leading ASO signal as its sole predictor, successfully predicts April PENA, thereby indicating that ASO is a key component of April PENA variability. Both the high correlation coefficient between March ASO and April PENA and our leave-one-out cross validation test confirm that ASO is a viable predictor for PENA, underscoring the potential for using Arctic ozone data to improve seasonal predictions of April precipitation.

Author Contributions: Conceptualization, X.M. and F.X.; methodology, X.M. and F.X.; software, X.M. and F.X.; validation, X.M., F.X., X.C., L.W., and G.Y.; formal analysis, X.M. and F.X.; investigation, X.M. and F.X.; writing—original draft preparation, X.M. and F.X.; writing—review and editing, X.M., F.X., X.C., L.W., and G.Y.; funding acquisition, F.X., X.C., L.W., and X.M. All authors have read and agreed to the published version of the manuscript.

Funding: This research was funded by the National Natural Science Foundation of China (42122037, 41975047, 41875047 and 12135003), Postdoctoral Innovative Talent Support Program of China (BX20220039).

Data Availability Statement: The dataset from SWOOSH for this study can be found at <https://csl.noaa.gov/groups/csl8/swoosh>, accessed on 9 October 2022. The dataset from GOZCARDS for this study can be found at <https://disc.gsfc.nasa.gov/datasets?keywords=GOZCARDS>, accessed on 9 October 2022. The dataset from GPCC for this study can be found at <https://psl.noaa.gov/data/gridded/data.gpcc.html>, accessed on 9 October 2022. The dataset from GPCP for this study can be found at <https://psl.noaa.gov/data/gridded/data.gpcp.html>, accessed on 9 October 2022. The NCEP2 data used in this study can be found at <https://psl.noaa.gov/data/gridded/data.ncep.reanalysis2.html>, accessed on 9 October 2022.

Acknowledgments: We acknowledge ozone datasets from the SWOOSH and GOZCARDS; precipitation from GPCC and GPCP; Meteorological fields from NCEP2. All the datasets are available online and can be downloaded for free. We thank NCAR for providing the CESM model.

Conflicts of Interest: The authors declare no conflict of interest.

References

1. Trenberth, K.E.; Jones, P.D.; Ambenje, P.; Bojariu, R.; Easterling, D.; Klein Tank, A.; Parker, D.; Rahimzadeh, F.; Renwick, J.A.; Rusticucci, M.; et al. Observations: Surface and Atmospheric Climate Change. In *Climate Change 2007: The Physical Science Basis*; Contribution of Working Group I to the Fourth Assessment Report of the Intergovernmental Panel on Climate Change; Solomon, S., Qin, D., Manning, M., Chen, Z., Marquis, M., Averyt, K.B., Tignor, M., Miller, H.L., Eds.; Cambridge University Press: Cambridge, UK; New York, NY, USA, 2007.
2. NOAA National Centers for Environmental Information (NCEI). *State of the Climate: Monthly Drought Report for April 2010*; NOAA/NCEI: Asheville, NC, USA, 2010.
3. NOAA National Centers for Environmental Information (NCEI). *State of the Climate: Monthly Drought Report for April 2011*; NOAA/NCEI: Asheville, NC, USA, 2011.
4. Stone, D.A.; Weaver, A.J.; Zwiers, F.W. Trends in Canadian precipitation intensity. *Atmos. Ocean* **2000**, *38*, 321–347. [[CrossRef](#)]
5. Zhang, X.B.; Hogg, W.D.; Mekis, E. Spatial and temporal characteristics of heavy precipitation events over Canada. *J. Clim.* **2001**, *14*, 1923–1936. [[CrossRef](#)]
6. Zhang, X.B.; Vincent, L.A.; Hogg, W.D.; Niitsoo, A. Temperature and precipitation trends in Canada during the 20th century. *Atmos. Ocean* **2000**, *38*, 395–429. [[CrossRef](#)]
7. Groisman, P.Y.; Knight, R.W.; Karl, T.R. Heavy precipitation and high streamflow in the contiguous United States: Trends in the twentieth century. *Bull. Am. Meteorol. Soc.* **2001**, *82*, 219–246. [[CrossRef](#)]
8. Zhang, X.B.; Harvey, K.D.; Hogg, W.D.; Yuzyk, T.R. Trends in Canadian streamflow. *Water Resour. Res.* **2001**, *37*, 987–998. [[CrossRef](#)]

9. Kunkel, K.E.; Andsager, K.; Liang, X.Z.; Arritt, R.W.; Takle, E.S.; Gutowski, W.J.; Pan, Z.T. Observations and regional climate model simulations of heavy precipitation events and seasonal anomalies: A comparison. *J. Hydrometeorol.* **2002**, *3*, 322–334. [[CrossRef](#)]
10. Small, D.; Islam, S.; Vogel, R.M. Trends in precipitation and streamflow in the eastern US: Paradox or perception? *Geophys. Res. Lett.* **2006**, *33*, 395–409. [[CrossRef](#)]
11. Vincent, L.A.; Mekis, E. Changes in daily and extreme temperature and precipitation indices for Canada over the twentieth century. *Atmos. Ocean* **2006**, *s44*, 177–193. [[CrossRef](#)]
12. Mekis, E.; Vincent, L.A. An Overview of the Second Generation Adjusted Daily Precipitation Dataset for Trend Analysis in Canada. *Atmos. Ocean* **2011**, *49*, 163–177. [[CrossRef](#)]
13. Griffiths, M.L.; Bradley, R.S. Variations of twentieth-century temperature and precipitation extreme indicators in the northeast United States. *J. Clim.* **2007**, *20*, 5401–5417. [[CrossRef](#)]
14. Brown, P.J.; Bradley, R.S.; Keimig, F.T. Changes in Extreme Climate Indices for the Northeastern United States, 1870–2005. *J. Clim.* **2010**, *23*, 6555–6572. [[CrossRef](#)]
15. Walsh, J.; Wuebbles, D.; Hayhoe, K.; Kossin, J.; Kunkel, K.; Stephens, G.; Thorne, P.; Vose, R.; Wehner, M.; Willis, J.; et al. Chapter 2: Our Changing Climate. In *Climate Change Impacts in the United States: The Third National Climate Assessment*; Global Change Research Program: Washington, DC, USA, 2014; pp. 19–67.
16. Agel, L.; Barlow, M.; Qian, J.H.; Colby, F.; Douglas, E.; Eichler, T. Climatology of Daily Precipitation and Extreme Precipitation Events in the Northeast United States. *J. Hydrometeorol.* **2015**, *16*, 2537–2557. [[CrossRef](#)]
17. Frei, A.; Kunkel, K.E.; Matonse, A. The Seasonal Nature of Extreme Hydrological Events in the Northeastern United States. *J. Hydrometeorol.* **2015**, *16*, 2065–2085. [[CrossRef](#)]
18. Huang, H.P.; Winter, J.M.; Osterberg, E.C.; Horton, R.M.; Beckage, B. Total and Extreme Precipitation Changes over the Northeastern United. *J. Hydrometeorol.* **2017**, *18*, 1783–1798. [[CrossRef](#)] [[PubMed](#)]
19. Montroy, D.L. Linear relation of central and eastern North American precipitation to tropical Pacific Sea surface temperature anomalies. *J. Clim.* **1997**, *10*, 541–558. [[CrossRef](#)]
20. Hartley, S.; Keables, M.J. Synoptic associations of winter climate and snowfall variability in New England, USA, 1950–1992. *Int. J. Climatol.* **1998**, *18*, 281–298. [[CrossRef](#)]
21. Kunkel, K.E.; Angel, J.R. Relationship of ENSO to snowfall and related cyclone activity in the contiguous United States. *J. Geophys. Res. Atmos.* **1999**, *104*, 19425–19434. [[CrossRef](#)]
22. Bradbury, J.A.; Keim, B.D.; Wak, C.P. The Influence of Regional Storm Tracking and Teleconnections on Winter Precipitation in the Northeastern United States. *Ann. Assoc. Am. Geog.* **2003**, *93*, 544–556. [[CrossRef](#)]
23. Shabbar, A. The impact of El Niño-Southern Oscillation on the Canadian climate. *Adv. Geophys.* **2006**, *6*, 149–153. [[CrossRef](#)]
24. Archambault, H.M.; Bosart, L.F.; Keyser, D.; Ayyer, A.R. Influence of large-scale flow regimes on cool-season precipitation in the northeastern United States. *Water Resour. Res.* **2008**, *136*, 2945–2963. [[CrossRef](#)]
25. Durkee, J.D.; Frye, J.D.; Fuhrmann, C.M.; Lacke, M.C.; Jeong, H.G.; Mote, T.L. Effects of the North Atlantic Oscillation on precipitation-type frequency and distribution in the eastern United States. *Theor. Appl. Climatol.* **2008**, *94*, 51–65. [[CrossRef](#)]
26. Gutzman, W.L. An Investigation of Broad-scale Vertical Motions and Precipitation in an Eastern North American Storm. *Water Resour. Res.* **2009**, *90*, 419. [[CrossRef](#)]
27. Ning, L.; Bradley, R.S. Winter precipitation variability and corresponding teleconnections over the northeastern United States. *J. Geophys. Res. Atmos.* **2014**, *119*, 7931–7945. [[CrossRef](#)]
28. Thiombiano, A.N.; St-Hilaire, A.; El Adlouni, S.E.; Ouarda, T.B.M.J. Nonlinear response of precipitation to climate indices using a non-stationary Poisson-generalized Pareto model: Case study of southeastern Canada. *Int. J. Climatol.* **2018**, *38*, E875–E888. [[CrossRef](#)]
29. Thiombiano, A.N.; El Adlouni, S.; St-Hilaire, A.; Ouarda, T.B.M.J.; El-Jabi, N. Nonstationary frequency analysis of extreme daily precipitation amounts in Southeastern Canada using a peaks-over-threshold approach. *Theor. Appl. Climatol.* **2017**, *129*, 413–426. [[CrossRef](#)]
30. Whan, K.; Zwiers, F. The impact of ENSO and the NAO on extreme winter precipitation in North America in observations and regional climate models. *Clim. Dyn.* **2017**, *48*, 1401–1411. [[CrossRef](#)]
31. Tan, X.Z.; Gan, T.Y.; Chen, Y.D. Synoptic moisture pathways associated with mean and extreme precipitation over Canada for winter and spring. *Clim. Dyn.* **2019**, *53*, 2663–2681. [[CrossRef](#)]
32. Trenberth, K.E. The definition of El Niño. *Bull. Am. Meteorol. Soc.* **1997**, *78*, 2771–2777. [[CrossRef](#)]
33. Hirsch, M.E.; DeGaetano, A.T.; Colucci, S.J. An East Coast winter storm climatology. *J. Clim.* **2001**, *14*, 882–899. [[CrossRef](#)]
34. Wallace, J.M.; Gutzler, D.S. Teleconnections in the Geopotential Height Field during the Northern Hemisphere Winter. *Water Resour. Res.* **1981**, *109*, 784–812. [[CrossRef](#)]
35. Leathers, D.J.; Yarnal, B.; Palecki, M.A. The Pacific North-American Teleconnection Pattern and United-States Climate. Part I: Regional Temperature and Precipitation Associations. *J. Clim.* **1991**, *4*, 517–528. [[CrossRef](#)]
36. Barnston, A.G.; Livezey, R.E. Classification, Seasonality and Persistence of Low-Frequency Atmospheric Circulation Patterns. *Water Resour. Res.* **1987**, *115*, 1083–1126. [[CrossRef](#)]
37. Schlesinger, M.E.; Ramankutty, N. An Oscillation in the Global Climate System of Period 65–70 Years. *Nature* **1994**, *367*, 723–726. [[CrossRef](#)]

38. Mantua, N.J.; Hare, S.R.; Zhang, Y.; Wallace, J.M.; Francis, R.C. A Pacific interdecadal climate oscillation with impacts on salmon production. *Bull. Am. Meteorol. Soc.* **1997**, *78*, 1069–1079. [[CrossRef](#)]
39. Calvo, N.; Polvani, L.M.; Solomon, S. On the surface impact of Arctic stratospheric ozone extremes. *Environ. Res. Lett.* **2015**, *10*, 094003. [[CrossRef](#)]
40. Ivy, D.J.; Solomon, S.; Calvo, N.; Thompson, D.W.J. Observed connections of Arctic stratospheric ozone extremes to Northern Hemisphere surface climate. *Environ. Res. Lett.* **2017**, *12*, 024004. [[CrossRef](#)]
41. Hu, Y.Y.; Tung, K.K. Possible ozone-induced long-term changes in planetary wave activity in late winter. *J. Clim.* **2003**, *16*, 3027–3038. [[CrossRef](#)]
42. Hu, Y.Y.; Tung, K.K.; Liu, J.P. A closer comparison of early and late-winter atmospheric trends in the northern hemisphere. *J. Clim.* **2005**, *18*, 3204–3216. [[CrossRef](#)]
43. Smith, K.L.; Polvani, L.M. The surface impacts of Arctic stratospheric ozone anomalies. *Environ. Res. Lett.* **2014**, *9*, 074015. [[CrossRef](#)]
44. Karpechko, A.Y.; Perlwitz, J.; Manzini, E. A model study of tropospheric impacts of the Arctic ozone depletion 2011. *J. Geophys. Res. Atmos.* **2014**, *119*, 7999–8014. [[CrossRef](#)]
45. Xie, F.; Li, J.P.; Tian, W.S.; Fu, Q.; Jin, F.F.; Hu, Y.Y.; Zhang, J.K.; Wang, W.K.; Sun, C.; Feng, J.; et al. A connection from Arctic stratospheric ozone to El Niño-southern oscillation. *Environ. Res. Lett.* **2016**, *11*, 124026. [[CrossRef](#)]
46. Hu, D.; Guan, Z.; Tian, W. Signatures of the Arctic stratospheric ozone in northern Hadley circulation extent and subtropical precipitation. *Geophys. Res. Lett.* **2019**, *46*, 12340–12349. [[CrossRef](#)]
47. Ma, X.; Xie, F.; Li, J.P.; Tian, W.S.; Ding, R.Q.; Sun, C.; Zhang, J.K. Effects of Arctic stratospheric ozone changes on spring precipitation in the northwestern United States. *Atmos. Chem. Phys.* **2019**, *19*, 861–875. [[CrossRef](#)]
48. Zhang, K.; Wang, T.; Xu, M.; Zhang, J. Influence of wintertime polar vortex variation on the climate over the north pacific during late winter and spring. *Atmosphere* **2019**, *10*, 670. [[CrossRef](#)]
49. Domeisen, D.I.V. Estimating the frequency of sudden stratospheric warming events from surface observations of the North Atlantic Oscillation. *J. Geophys. Res. Atmos.* **2019**, *124*, 3180–3194. [[CrossRef](#)]
50. Dunn-Sigouin, E.; Shaw, T.A. Comparing and contrasting extreme stratospheric events, including their coupling to the tropospheric circulation. *J. Geophys. Res. Atmos.* **2015**, *120*, 1374–1390. [[CrossRef](#)]
51. Kidston, J.; Scaife, A.A.; Hardiman, S.C.; Mitchell, D.M.; Butchart, N.; Baldwin, M.P.; Gray, L.J. Stratospheric influence on tropospheric jet streams, storm tracks and surface weather. *Nat. Geosci.* **2015**, *8*, 433–440. [[CrossRef](#)]
52. King, A.D.; Butler, A.H.; Jucker, M.; Earl, N.O.; Rudeva, I. Observed relationships between sudden stratospheric warmings and European climate extremes. *J. Geophys. Res. Atmos.* **2019**, *124*, 13943–13961. [[CrossRef](#)]
53. Orsolini, Y.J.; Nishii, K.; Nakamura, H. Duration and decay of Arctic stratospheric vortex events in the ECMWF seasonal forecast model. *Q. J. Roy. Meteor. Soc.* **2018**, *144*, 2876–2888. [[CrossRef](#)]
54. Tripathi, O.P.; Charlton-Perez, A.; Sigmond, M.; Vitart, F. Enhanced long-range forecast skill in boreal winter following stratospheric strong vortex conditions. *Environ. Res. Lett.* **2015**, *10*, 104007. [[CrossRef](#)]
55. Zhang, J.; Zheng, H.; Xu, M.; Yin, Q.; Zhao, S.; Tian, W.; Yang, Z. Impacts of stratospheric polar vortex changes on wintertime precipitation over the northern hemisphere. *Clim. Dyn.* **2022**, *58*, 3155–3171. [[CrossRef](#)]
56. Cheung, J.C.H.; Haigh, J.D.; Jackson, D.R. Impact of EOS MLS ozone data on medium-extended range ensemble weather forecasts. *J. Geophys. Res. Atmos.* **2014**, *119*, 9253–9266. [[CrossRef](#)]
57. Stone, K.A.; Solomon, S.; Kinnison, D.E.; Baggett, C.F.; Barnes, E.A. Prediction of Northern Hemisphere Regional Surface Temperatures Using Stratospheric Ozone Information. *J. Geophys. Res. Atmos.* **2019**, *124*, 5922–5933. [[CrossRef](#)]
58. Xie, F.; Ma, X.; Li, J.P.; Tian, W.S.; Ruan, C.Q.; Sun, C. Using Observed Signals from the Arctic Stratosphere and Indian Ocean to Predict April-May Precipitation in Central China. *J. Clim.* **2020**, *33*, 131–143. [[CrossRef](#)]
59. Davis, S.M.; Rosenlof, K.H.; Hassler, B.; Hurst, D.F.; Read, W.G.; Vömel, H.; Selkirk, H.; Fujiwara, M.; Damadeo, R. The Stratospheric Water and Ozone Satellite Homogenized (SWOOSH) database: A long-term database for climate studies. *Earth Syst. Sci. Data* **2016**, *8*, 461–490. [[CrossRef](#)]
60. Froidevaux, L.; Anderson, J.; Wang, H.J.; Fuller, R.A.; Schwartz, M.J.; Santee, M.L.; Livesey, N.J.; Pumphrey, H.C.; Bernath, P.F.; Russell III, J.M.; et al. Global Ozone Chemistry And Related trace gas Data records for the Stratosphere (GOZCATS): Methodology and sample results with a focus on HCl, H₂O, and O₃. *Atmos. Chem. Phys.* **2015**, *15*, 10471–10507. [[CrossRef](#)]
61. Xie, F.; Li, J.P.; Zhang, J.K.; Tian, W.S.; Hu, Y.Y.; Zhao, S.; Sun, C.; Ding, R.Q.; Feng, J.; Yang, Y. Variations in North Pacific sea surface temperature caused by Arctic stratospheric ozone anomalies. *Environ. Res. Lett.* **2017**, *12*, 114023. [[CrossRef](#)]
62. Huffman, G.J.; Adler, R.F.; Arkin, P.; Chang, A.; Ferraro, R.; Gruber, A.; Janowiak, J.; McNab, A.; Rudolf, B.; Schneider, U. The Global Precipitation Climatology Project (GPCP) Combined Precipitation Dataset. *Bull. Am. Meteorol. Soc.* **1997**, *78*, 5–20. [[CrossRef](#)]
63. Schneider, U.; Finger, P.; Meyer-Christoffer, A.; Rustemeier, E.; Ziese, M.; Becker, A. Evaluating the Hydrological Cycle over Land Using the Newly-Corrected Precipitation Climatology from the Global Precipitation Climatology Centre (GPCC). *Atmosphere* **2017**, *8*, 52. [[CrossRef](#)]
64. Hersbach, H.; Bell, B.; Berrisford, P.; Hirahara, S.; Thépaut, J. The ERA5 global reanalysis. *Q. J. Roy. Meteor. Soc.* **2020**, *146*, 1999–2049. [[CrossRef](#)]

65. Kanamitsu, M.; Ebisuzaki, W.; Woollen, J.; Yang, S.K.; Hnilo, J.J.; Fiorino, M.; Potter, G.L. NCEP-DOE AMIP-II reanalysis (R-2). *Bull. Am. Meteorol. Soc.* **2002**, *83*, 1631–1643. [[CrossRef](#)]
66. Marsh, D.R.; Mills, M.J.; Kinnison, D.E.; Lamarque, J.F.; Calvo, N.; Polvani, L.M. Climate Change from 1850 to 2005 Simulated in CESM1(WACCM). *J. Clim.* **2013**, *26*, 7372–7391. [[CrossRef](#)]
67. Garcia, R.R.; Marsh, D.R.; Kinnison, D.E.; Boville, B.A.; Sassi, F. Simulation of secular trends in the middle atmosphere, 1950–2003. *J. Geophys. Res. Atmos.* **2007**, *112*, D09301. [[CrossRef](#)]
68. WMO (World Meteorological Organization). Scientific Assessment of Ozone depletion: 2002. In *Global Ozone Research and Monitoring Project, Report No. 47*; World Meteorological Organization: Geneva, NY, USA, 2003; p. 498.
69. Luo, S.Z.; Wang, C.; Xi, X.H.; Pan, F.F. Estimating FPAR of maize canopy using airborne discrete-return LiDAR data. *Opt. Express* **2014**, *22*, 5106–5117. [[CrossRef](#)]
70. Efron, B. *The Jackknife, the Bootstrap and Other Resampling Plans*. Society for Industrial and Applied Mathematics; SIAM: Philadelphia, PA, USA, 1982.
71. Guo, Y.; Li, J.P.; Li, Y. A Time-Scale Decomposition Approach to Statistically Downscale Summer Rainfall over North China. *J. Clim.* **2012**, *25*, 572–591. [[CrossRef](#)]
72. Zorita, E.; von Storch, H. The analog method as a simple statistical downscaling technique: Comparison with more complicated methods. *J. Clim.* **1999**, *12*, 2474–2489. [[CrossRef](#)]
73. Xie, F.; Ma, X.; Li, J.P.; Huang, J.L.; Tian, W.S.; Zhang, J.K.; Hu, Y.Y.; Sun, C.; Zhou, X.; Feng, J.; et al. An advanced impact of Arctic stratospheric ozone changes on spring precipitation in China. *Clim. Dyn.* **2018**, *51*, 4029–4041. [[CrossRef](#)]
74. Ma, X.; Xie, F. Predicting April Precipitation in the Northwestern United States Based on Arctic Stratospheric Ozone and Local Circulation. *Front. Earth Sci.* **2020**, *8*, 56. [[CrossRef](#)]
75. Ramaswamy, V.; Schwarzkopf, M.D.; Randel, W.J. Fingerprint of ozone depletion in the spatial and temporal pattern of recent lower-stratospheric cooling. *Nature* **1996**, *382*, 616–618. [[CrossRef](#)]
76. Hu, Y.Y.; Xia, Y.; Fu, Q. Tropospheric temperature response to stratospheric ozone recovery in the 21st century. *Atmos. Chem. Phys.* **2011**, *11*, 7687–7699. [[CrossRef](#)]
77. Wang, T.; Tian, W.; Zhang, J.; Xu, M.; Lian, T.; Hu, D.; Qie, K. Surface ocean current variations in the north pacific related to arctic stratospheric ozone. *Clim. Dyn.* **2022**, *59*, 3087–3111. [[CrossRef](#)]
78. Kunkel, K.E.; Stevens, S.E.; Stevens, L.E.; Karl, T.R. Observed climatological relationships of extreme daily precipitation events with precipitable water and vertical velocity in the contiguous United States. *Geophys. Res. Lett.* **2020**, *47*, e2019GL086721. [[CrossRef](#)]
79. Wang, W.; Seaman, N.L. A Comparison Study of Convective Parameterization Schemes in a Mesoscale Model. *Water Resour. Res.* **1997**, *125*, 252–278. [[CrossRef](#)]
80. Wang, Y.C.; Pan, H.L.; Hsu, H.H. Impacts of the triggering function of cumulus parameterization on warm-season diurnal rainfall cycles at the Atmospheric Radiation Measurement Southern Great Plains site. *J. Geophys. Res. Atmos.* **2015**, *120*, 10681–10702. [[CrossRef](#)]
81. Gao, Y.; Leung, L.R.; Zhao, C.; Hagos, S. Sensitivity of U.S. summer precipitation to model resolution and convective parameterizations across gray zone resolutions. *J. Geophys. Res. Atmos.* **2017**, *122*, 2714–2733. [[CrossRef](#)]
82. Kim, M.K.; Kang, I.S.; Park, C.K.; Kim, K.M. Super ensemble prediction of regional precipitation over Korea. *Int. J. Climatol.* **2004**, *24*, 777–790. [[CrossRef](#)]